Monolithically Integrating III-Nitride Quantum Structure for Full-Spectrum White LED via Bandgap Engineering Heteroepitaxial Growth

Author Manuscript

*Benjie Fan, Xiaoyu Zhao, Jingqiong Zhang, Yuechang Sun, Hongzhi Yang, L. Jay Guo, and Shengjun Zhou**

B. J. Fan, J. Q. Zhang, H. Z. Yang

Kaistar Lighting (Xiamen) Co., Ltd., Xiamen 361000, P. R. China

X. Y. Zhao, Y. C. Sun, S. J. Zhou
Center for Photonics and Semiconductors, School of Power and Mechanical Engineering, Wuhan University, Wuhan 430072, P. R. China

E-mail: zhousj@whu.edu.cn

L. J. Guo

Department of Electrical Engineering and Computer Science, University of Michigan,

Ann Arbor, MI, 48109, USA

Keywords: Bandgap engineering heteroepitaxial growth, carrier distribution rearrangement, trichromatic multiple quantum wells, full-spectrum white LED, color rendering

This is the author manuscript accepted for publication and has undergone full peer review but has not been through the copyediting, typesetting, pagination and proofreading process, which may lead to differences between this version and the Version of Record. Please cite this article as doi: 10.1002/lpor.202200455.

This article is protected by copyright. All rights reserved.

Great progress made by heteroepitaxial growth technology encourages rapid development of III-nitride heteroepitaxial structures and their applications in extensive fields. Particularly, innate bandgap tunability of III-nitride materials renders them attractive for white light-emitting diodes (WLEDs) that are considered as next-generation solid-state lighting sources. However, commercial phosphor-converted WLEDs suffer from poor color rendering index (CRI) and intense blue component, hard to fulfill demanding requirements simultaneously for energy efficiency and healthy lighting. Here, we report an efficient full-spectrum WLED excited by monolithically integrated III-nitride quantum structure, in which trichromatic InGaN/GaN multiple quantum wells have been constructed by bandgap engineering heteroepitaxy growth allowing flexible regulation of indium composition and quantum barrier thickness to manipulate carrier transport behavior. Furthermore, relationship between structural parameters and emission characteristics as well as their impact on white light performance has been systematically demonstrated. Combined with commonly used green-red phosphor mixture, the fabricated full-spectrum warm/cold WLEDs can emit broadband and continuous spectra with low-ratio blue component, first exhibiting superior CRI (> 97/98), color fidelity (97/97), saturation (100/99) and luminous efficacy (>120/140 lm/W). This work demonstrates the advantages of bandgap-engineered quantum structure applied in excitation source, and opens up new avenues for the exploration of high-quality solid-state lighting.

1. Introduction

The past few decades of technological advances in heteroepitaxial growth have witnessed widespread applications of III-nitride electronic or optoelectronic devices on heterogeneous substrate [1]. Metal-organic chemical vapor deposition (MOCVD), as a standard bottom-up epitaxial growth technology, has been widely utilized for III-nitride films [2], metal oxides [3], and transition metal dichalcogenides [4]. The intrinsic properties of wide and tunable bandgap that covers the entire visible spectra make III-nitride semiconductors compelling candidates for realizing high-performance white light-emitting diodes (WLEDs) [5]. Owing to their merits including high efficiency, long lifetime, and substantial energy savings, III-nitride WLEDs have been considered as a promising replacement of traditional incandescent and fluorescent lamps to solve the increasingly prominent energy shortage and carbon emission issues [6]. Nowadays, commercial WLEDs are mainly fabricated by utilizing InGaN blue LED chip with $Y_3Al_5O_{12}$: Ce^{3+} (YAG: Ce^{3+}) yellow phosphor [7]. However, limited by red component as well as cyan gap between blue and yellow emission, this strategy results in a low CRI (R_a < 80), high correlated color temperature (CCT > 4500 K) and especially blue-light hazard, unsuitable for demanding applications and even detrimental for human health [8]. By contrast,

Author Manuscript

This article is protected by copyright. All rights reserved.

sunlight that features continuous and broadband spectra is considered the most ideal for individuals from both practical and photobiologically friendly aspects. In this regard, natural sunlight-like lighting sources are highly desirable to satisfy the booming demand for healthy lighting that has attracted enormous interest [9].

Apart from great efforts to develop efficient color convertors including phosphors and quantum dots [10], the critical role played by excitation source structure in WLED performance cannot be ignored. The pioneering researches, which were conducted by Akasaki, Amano and Nakamura, pave a considerably important way to achieve efficient III-nitride LEDs as excitation source [11]. By means of MOCVD technology, one can facilely engineer the III-nitride heterostructure from nanoscale perspective, allowing high degrees of freedom to manipulate carrier transport behavior and thus to govern the emission characteristics. InGaN/GaN multiple quantum wells (MQWs) active region, where carriers distribute and participate in the recombination process, acts as a core component whose quantum structural parameters (indium composition, thickness and sequence of InGaN QWs, thickness and doping of GaN quantum barriers) have been reported to affect carrier transport and corresponding device properties by experiments and numerical simulations [12]. Despite fundamental importance of MQWs active region, few research has been conducted to adjust its quantum structure applied in excitation source and to explore the physical mechanism. Thus, rational optimization of active region by bandgap engineering heteroepitaxial growth holds great promise for yielding high-quality white light.

In this work, we develop efficient sunlight-like WLEDs where the excitation sources possess monolithically integrated III-nitride quantum structure with varying indium compositions and quantum barrier widths on sapphire by bandgap engineering heteroepitaxial growth. The characterization of optoelectronic properties and crystalline quality demonstrates that our proposed bandgap-engineered LED structure yields trichromatic emission while maintaining similar crystalline quality and light output power as the monochromatic LED structure. According to numerical simulation, we compare the carrier transport behavior in the active region of these two epitaxial structures and find the carrier distribution rearrangement in different indium-composition epilayers. This contributes to broadband and continuous spectra suitable for both warm and cold white light emission, confirming the reasonability and superiority of bandgap engineering heteroepitaxial

Author Manuscript

This article is protected by copyright. All rights reserved.

growth. In particular, tailoring wavelength interval and intensity ratio of trichromatic LED allows for further promotion in white light characteristics. The fabricated full-spectrum WLEDs excited by III-nitride trichromatic LEDs display superior color rendering of 97.5/98.9, color fidelity of 97/97, saturation of 100/99 and simultaneously high luminous efficacy around 124/145 lm/W at low CCT (2700~3000 K)/high CCT (4800 K~5100 K) operating at 60 mA, respectively. To our best knowledge, these record values are simultaneously realized for phosphor-converted WLED excited by trichromatic excitation source for the first time. Our study establishes a universal strategy to monolithically integrate efficient sunlight-like WLEDs on sapphire, aiming for high-quality lighting sources.

2. Result and Discussion

2.1 Comparison of Monochromatic and Trichromatic MQWs and Their Application for WLEDs

The schematic epitaxial structure of GaN-based LEDs is shown in **Figure 1a** and the detailed structure parameters are provided in Experimental Section. Noteworthy, compared to the monochromatic LED (MLED) with uniform indium composition in InGaN/GaN MQWs, our specially designed trichromatic LEDs (TLEDs) have different indium compositions in MQWs, corresponding to emission wavelengths λ_{Peak1} (445~470 nm), λ_{Peak2} (430~450 nm) and λ_{Peak3} (425~435 nm). The detailed schematic of band diagram for TLEDs is shown in Figure 1b. Cmpared to the 1st and 3rd-6th QWs with emission of λ_{Peak2}, the 2nd QW with emission of λ_{Peak1} has relatively narrower bandgap , while the 7th–9th QWswith emission of λ_{Peak3} have relatively wider bandgap. The indium composition of MQWs in MLED and TLED is characterized using secondary ion mass spectrometry (SIMS), as shown in Figure 1c. Obviously, uniform indium composition can be seen for MLED, whereas there exist three different indium compositions in TLED, in agreement with our design expectations. High resolution X-ray diffraction (HRXRD) ω-2ϑ scan was performed to characterize the crystalline quality for both samples. The dominant peak arises from the GaN (002) plane and satellite peaks arise from InGaN/GaN MQWs [13]. In Figure 1d, high order satellite peaks can be clearly observed for MLED and TLED, which indicates the fine layer periodicity and sharp interfaces of MQWs [14]. This is also

Author Manuscript

This article is protected by copyright. All rights reserved.

confirmed by the cross-sectional bright-field transmission electron microscopy (TEM) image of InGaN/GaN MQWs in TLED (Figure 1e).

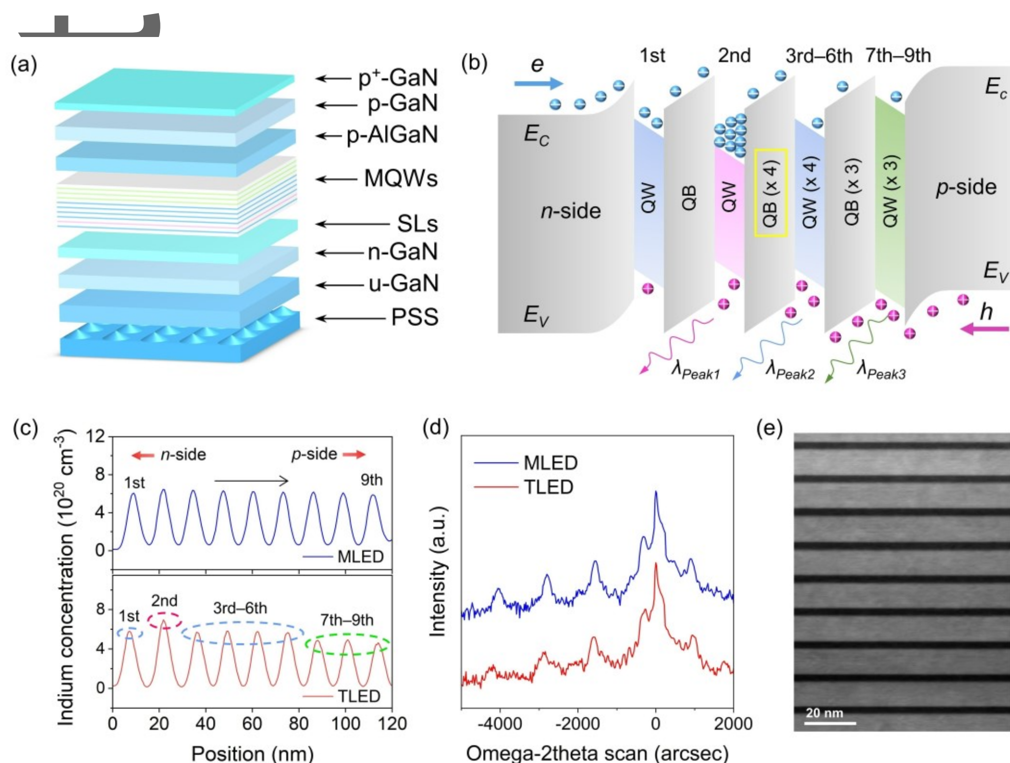

Figure 1. a) Schematic illustration for GaN-based trichromatic LED structure and b) corresponding energy band diagram of InGaN/GaN MQWs. c) SIMS profile of the indium concentration of InGaN/GaN MQWs as a function of position for MLED and TLED. d) XRD ω-2ϑ scan curves for MLED and TLED. e) Cross-sectional TEM image of InGaN/GaN MQWs in TLED.

We now compare the optoelectronic characteristics of MLED and TLED to investigate the applicability of trichromatic excitation source for white lighting. **Figure 2a** shows the electroluminescence (EL) spectra of MLED and TLED operating at 60 mA. We observe that MLED exhibits single peak (~450 nm), whereas TLED exhibits three peaks including two dominant peaks (~440 nm and ~456 nm) and a weak peak (~430 nm), originating from MQWs with different indium compositions. To reveal the correlation between structural parameter and emission characteristics, carrier transport behavior in MQWs is analyzed through numerical simulation. Figure 2b presents

This article is protected by copyright. All rights reserved.

the energy band profile of MQWs for MLED and TLED, together with the simulated electron and hole distribution shown in Figure 2c and 2d, respectively. According to the electron concentration distribution profiles, we find that electrons mainly accumulate in the 1st QW for MLED, while they show a quite different behavior for TLED. Since narrow-bandgap QW enhances the confinement of carriers, high electron concentration is observed in the 2nd QW for TLED. Meanwhile, electrons easily transport through wider-bandgap QWs due to the weak confinement effect, resulting in lower electron concentration in the 7th–9th QWs for TLED compared to that in the 7th–9th QWs for MLED. For III-nitride materials, holes have a larger effective mass and lower mobility than electrons [6c], so holes tend to accumulate near the p-GaN side. This is the case for MLED shown in Figure 2d. In contrast, wide-bandgap QWs are intentionally located near p-side for TLED, which favors the injection of holes into the high-indium-composition QW. Similar phenomenon has also been reported by other researchers [12b]. As a result, there exists high hole concentration in the 2nd QW for TLED. Such electron and hole distribution arises from the change in carrier confinement capability for QWs with different indium compositions, which in turn affects the radiative recombination in QWs corresponding to different peaks (Figure S2). The radiative recombination in QWs further contributes to different EL emission intensities of three peaks. That is to say, our specially designed structure enables the rearrangement of carriers in the entire InGaN/GaN MQWs of TLED, eventually resulting in the observed EL emission characteristics.

Figure 2e shows the light output power (LOP) versus current characteristics of MLED and TLED. It can be seen that MLED and TLED show almost identical LOP values at injection current below 150 mA. Besides, the current versus voltage curves are plotted in Figure 2f. We find that TLED shows relatively higher forward voltage compared to MLED at the same injection current. As the epitaxial structure for two samples is the same except the active region, variation in voltage-current curve is related to different active region structures. We suggest that different indium compositions of QWs in MLED and TLED may be the reason. Since indium compositions of QWs in TLED are lower than those of QWs in MLED (except the 2nd QW), the bandgaps of QWs in TLED are wider than those of QWs in MLED (except the 2nd QW), leading to an increase in forward voltage for TLED [15].

Author Manuscript

This article is protected by copyright. All rights reserved.

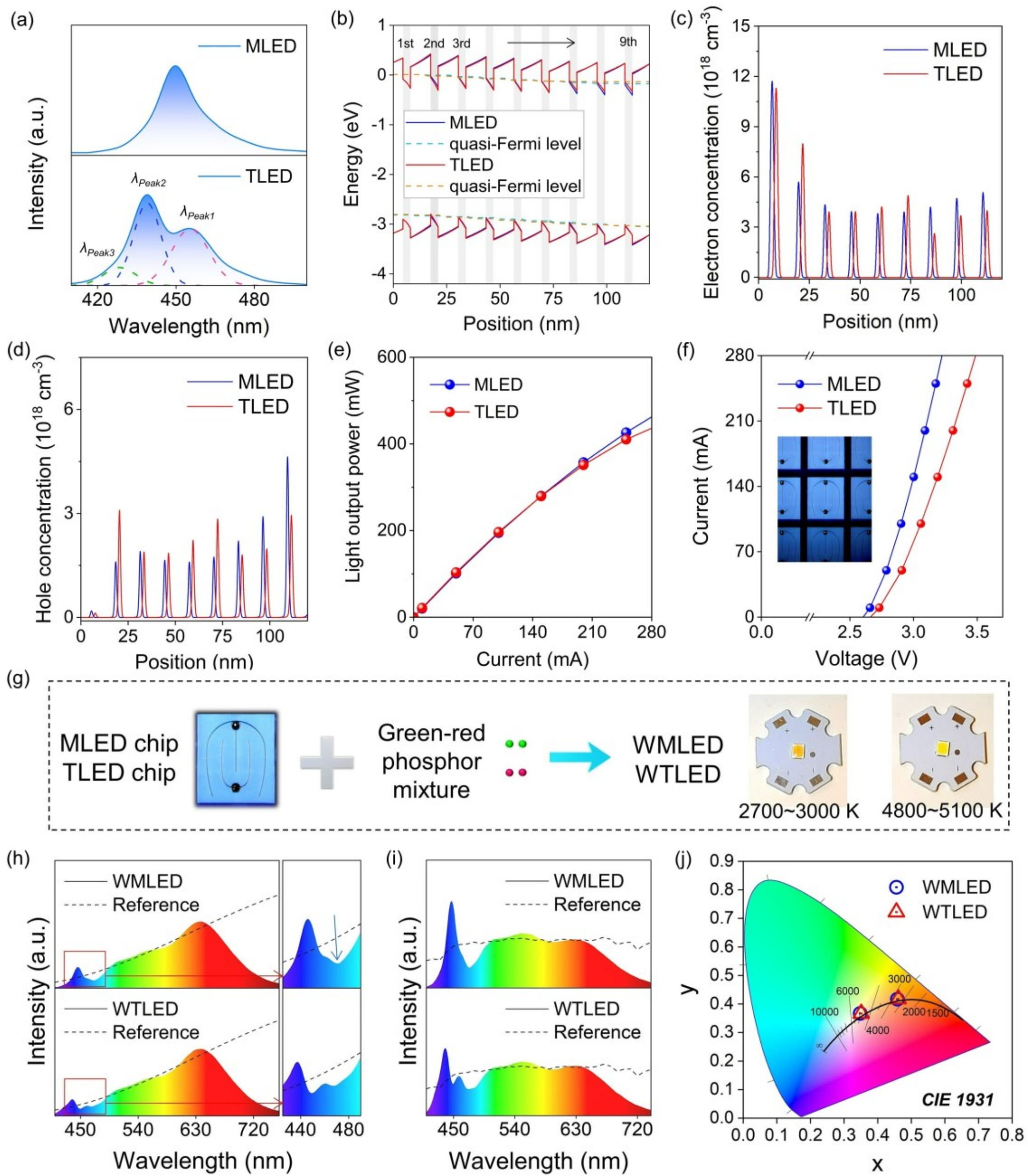

Figure 2. a) EL spectra of MLED and TLED. b) Energy band diagram of the MQWs for MLED and TLED. Numerical simulation of c) electron concentration and d) hole concentration of MLED and TLED. The electron and hole concentration profiles were purposely shifted by 2 nm for comparison. e) Experimental LOP versus current characteristics of the MLED and TLED. f) The current versus voltage characteristics of MLED and TLED. Inset: as-fabricated LED chip. g) Schematic diagram of the WMLED and WTLED fabrication. EL spectra of WMLED and WTLED with h) warm and i) cold white light

Autho

This article is protected by copyright. All rights reserved.

emission. j) CIE 1931 diagram showing the chromaticity coordinates of WMLED and WTLED with warm and cold white light emission.

Next, the aforementioned MLED and TLED were used as the excitation source and precoated with a green-red phosphor mixture to produce white light emission with CCT of 2700~3000 K and 4800~5100 K. These CCT values are chosen since they are typically representative of warm and cold light emission, advantageous for verifying the feasibility of our design. Figure 2h shows the warm white light emission spectra of MLED-excited WLED (WMLED) and TLED-excited WLED (WTLED). It could be seen that there exists an intense blue component in the WMLED spectra, indicating that a considerable part of blue light from the excitation source is not converted to other wavelength emission. Besides, the blue component is accompanied by a gap at ~470 nm (indicated by blue arrow in enlarged view of Figure 2h), which makes emission profile deviate from the blackbody radiation curve at short wavelengths. As for WTLED, not only the blue component intensity decreases, but the gap at ~470 nm is remedied, making the emission profile closer to the blackbody radiation curve. Moreover, the impact of excitation source on cold white light spectra is more evident in Figure 2i. Thus, we believe that compared to MLED, two additional peaks in TLED favor the continuity of spectra profile of WLEDs at short wavelengths, which is expected to mimic sunlight. Commission Internationale de l'éclairage (CIE) coordinates of the fabricated WLED samples almost lie on the Planckian locus, reconfirming the outstanding emission performance, as seen in Figure 2j. Other experimental results of WLEDs performance are summarized in Table S1. Especially, luminous efficacies of warm and cold WTLEDs are 125.60 and 152.58 lm/W, respectively, which are competitive with those of WMLEDs at corresponding CCT. This implies that utilizing TLED structure to fabricate WLEDs will not deteriorate the device luminous efficacy, which is appropriate for lighting applications.

2.2. Indium Composition Adjustment in Trichromatic MQWs and Their Application for WLEDs

Author Manuscript

This article is protected by copyright. All rights reserved.

As previously discussed, our proposed trichromatic MQWs structure can act as an alternative excitation source for full-spectrum WLEDs. We now investigate effect of structural parameters of trichromatic MQWs on emission properties of LEDs. Via bandgap engineering heteroepitaxial growth, we adjust indium composition in 2nd and 3rd–6th QWs of TLEDs to obtain different wavelength intervals ($\Delta\lambda$) between λ_{Peak1} and λ_{Peak2}. TLEDs with $\Delta\lambda$ of 16~18 nm, 21~23 nm and 26~28 nm are denoted as TLED A, B and C, respectively. **Figure 3a** presents the EL spectra of TLEDs. We utilized TLED A, B and C as the excitation source for WTLED A, B and C. For warm white light emission (Figure 3b), we observe that with the increasing $\Delta\lambda$, a gap (at 450~460 nm) becomes more obvious associated by gradually intense peak (at 470~480 nm), making emission spectra of warm white light deviate from the reference lighting source. For cold white light emission (Figure 3c), λ_{Peak1} and λ_{Peak2} of WTLEDs show different tends with the increasing $\Delta\lambda$. This makes the in-depth investigation necessary to explore the link between wavelength interval and white light characteristics.

Author Manuscript

This article is protected by copyright. All rights reserved.

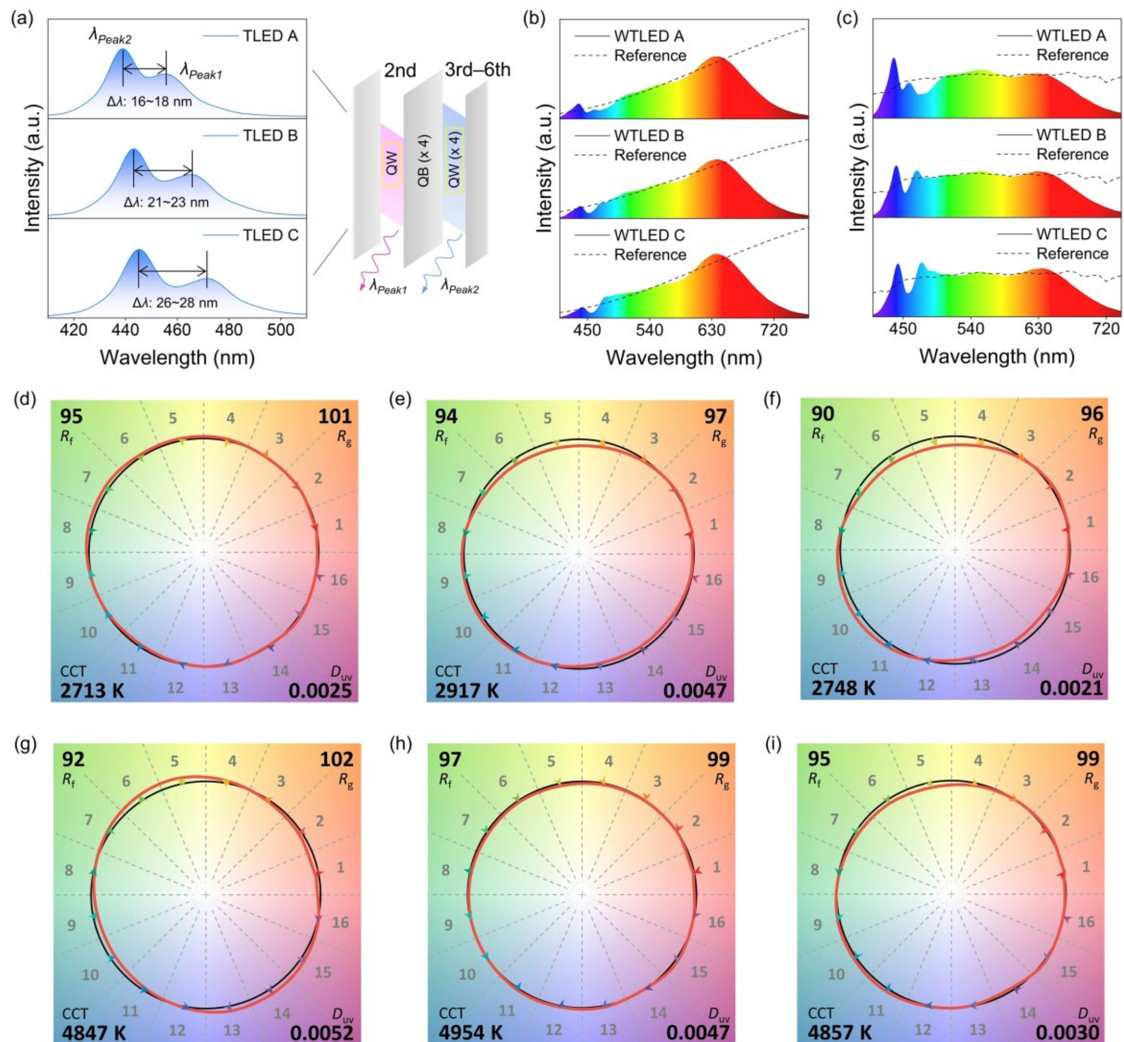

Figure 3. a) EL spectra of TLEDs with different Δλ. EL spectra of corresponding WTLED A, B and C with b) warm and c) cold white light emission. d)–f) CVGs of warm WTLED A, B and C. g)–i) CVGs of cold WTLED A, B and C.

As reported previously, CRI (R_a) is used to assess the ability of lighting sources to reproduce the color accurately when compared to the reference lighting source, which is either a Planckian radiator for CCT below 5000 K or daylight for CCT above 5000 K [16]. The general CRI corresponds to the average of the first eight CRIs (R_1–R_8) [17], while R_9 together with R_{10}–R_{15} define the special CRI [16].

This article is protected by copyright. All rights reserved.

Author Manuscript

Here, fifteen CRI points of these WTLEDs with warm and cold white light emission are provided in Figure S3a and S3b, respectively. For warm white light emission, we observe that WTLED A and B excited by TLEDs with relatively smaller $\Delta\lambda$ have higher R_a compared to WTLED C. Meanwhile, all CRI points of WTLED A and B are above 90. However, for cold white light emission, R_a of WTLED A (R_a = 91.6) is inferior to that of WTLED B (R_a = 98.9) and C (R_a = 95.9), implying that TLED with smaller $\Delta\lambda$ contributes to better warm light emission, whereas TLED with large $\Delta\lambda$ can greatly benefit cold light emission. In addition, luminous efficacy of WTLED C is the lowest among these three samples at both low and high CCT (Table S2). This can be attributed to longer λ_{Peak1}, which deviates from the dominant excitation region for green-red phosphors. In this regard, we should simultaneously consider the issues with respect to CRI and luminous efficacy and make a reasonable compromise. More impressively, there is a trade-off between CRI and luminance efficacy of radiation (LER) that can be expressed as [12a, 17],

$$F_{\sigma}(\lambda_1, \ldots, \lambda_n, \Delta\lambda_1, \ldots, \Delta\lambda_n, I_1, \ldots, I_n) = \sigma LER + (1-\sigma)CRI \quad (1)$$

where σ is a weighting factor ($0 \leq \sigma \leq 1$), and n is number of primary LEDs. λ_i, $\Delta\lambda_i$, and I_i represent peak wavelengths, spectral line widths, and the luminous fluxes, respectively. Considering that increasing LED chip number provides better CRI but deteriorates the LER of devices, our proposed monolithic LED strategy is demonstrated to be an effective and facile solution for solving this problem.

Since the CIE method was introduced in 1960 and modified in 1974 [18], it has been widely accepted and used to evaluate the color rendering ability. Nevertheless, this method is limited by the nonuniform color space, low saturated color samples, etc. [19], thus encouraging the development of alternative methods. Recently, the Illuminating Engineering Society (IES) reported a new two-measure system, describing a color fidelity index (CFI, R_f) and a color gamut index (CGI, R_g) defined as technical memorandum TM-30 [20]. In the TM-30 standard, a set of 99 real test samples with color space uniformity and spectral uniformity are used to assess WLED performance. Herein, besides the R_a values, we further use TM-30 method for more accurate evaluation of the color rendition of lighting sources. Color vector graphics (CVGs) of WTLEDs are provided in Figure 3d–3i. The arrows indicate the average color shifts of 16 hue bins induced by WTLEDs (red circle) relative to

This article is protected by copyright. All rights reserved.

those of reference lighting source (black circle). For warm white light emission (Figure 3d–3f), WTLED A shows slight oversaturation of green color, while WTLED B and C show undersaturation of green-yellow and violet-blue colors. For cold white light emission (Figure 3g–3i), slight oversaturation of green-yellow colors appears in the CVG of WTLED A, and slight undersaturation of green-yellow colors appears in the CVG of WTLED B and C.

Figure S4a and S4b show the R_g–R_f space plots of warm and cold WTLED samples to identify the impact of TLEDs with different $\Delta\lambda$ on the light quality. If (R_f, R_g) value of a lighting source is located in the preferred triangular zone within the ranges of R_f>90 and 90≤R_g≤110, such lighting source can be assumed to potentially approach the reference lighting source, whose (R_f, R_g) value is (100, 100) [21]. For warm white light, we find that WTLED A and B display (R_f, R_g) values of (95, 101) and (94, 97), respectively, which are located in the preferred triangular zone (Figure S4a). For cold white light, (R_f, R_g) values of WTLED B and C are (97, 99) and (95, 99), respectively, showing almost ideal fidelity and saturation (Figure S4b). Besides, D_{uv} value, which describes CCT value shift of emission from lighting source relative to the corresponding Planckian locus radiation, is quite low for all these samples, in excellent agreement with the chromaticity coordinates in Table S2. Therefore, these observations suggest that sunlight-like emission with excellent fidelity and saturation could be achieved by utilizing TLEDs with small $\Delta\lambda$ for warm white light and TLEDs with large $\Delta\lambda$ for cold white light.

2.3. Quantum Barrier Thickness Adjustment in Trichromatic MQWs and Their Application for WLEDs

Here we focus on the effect of QB structure on carrier transport and distribution characteristics [12e, 22]. Previous work has experimentally demonstrated that decreasing QB thickness facilitates the hole injection into MQWs near the *n*-GaN side [12e]. To change the intensity ratio of λ_{Peak1} to λ_{Peak2}, we modify the QB thickness of TLEDs (QBs adjacent to the 3rd–6th QWs). With the QB thickness decreasing (11.4, 10.5, 9.5 and 8.6 nm for TLED D, E, A, F, respectively), intensity ratio of λ_{Peak1} to λ_{Peak2} increases (~0.2, 0.4, 0.6 and 0.8), as seen in **Figure 4a.** To identify the physical mechanism for the dependence of intensity ratio on QB thickness, we present the energy band diagram of trichromatic MQWs (Figure 4b) and carrier concentration profile (Figure 4c) based on the numerical

Author Manuscript

This article is protected by copyright. All rights reserved.

simulation. First, increasing QB thickness results in the enhanced confinement for electrons and, thus, the increased electron concentration in 3rd–6th QWs corresponding to λ_{Peak2}. Second, due to the poor mobility of holes, increased QB thickness makes holes difficult to transport into QWs near n-side. As a result, holes tend to distribute in the 3rd–6th QWs corresponding to λ_{Peak2}, and a significant reduction of hole concentration is observed in the 2nd QW corresponding to λ_{Peak1}, leading to the intensity ratio variation in EL spectra. We plotted the measured intensity ratio as a function of QB thickness in Figure 4d.

We name WLEDs excited by TLED D, E, A and F as WTLED D, E, A and F, respectively. As presented in Figure S5a, emission spectra for WTLED D shows a strong blue component with a gap, which causes the deviation from reference lighting source. As the intensity ratio of λ_{Peak1} to λ_{Peak2} increases from 0.2 to 0.8, blue component is gradually reduced and meanwhile the wavelength gap is complemented for continuous emission at low CCT. This finding gets remarkable at high CCT (Figure S5b). Additionally, R_a values increase from 94.7 (WTLED D) to 97.5 (WTLED F) at low CCT. This means that color reproduction ability is improved with increasing intensity ratio (Table S3). Similar, but more pronounced trend is observed for WTLEDs with CCT of ~5000 K. These results confirm that emission spectra of WTLEDs are closer to reference lighting source as the intensity ratio increases. We summarized the CIE coordinates and CCTs of the fabricated WTLEDs (Table S3).

Furthermore, we present R_f–R_g values of WTLED D, E, A and F with cold and warm white light emission, as seen in Figure 4e and 4f, respectively. We find that increasing intensity ratio of TLEDs enables R_f of WTLEDs increase from 90 to 97 and from 84 to 94 for warm and cold white light emission, respectively. Besides, at low CCT, R_g for WTLED D and E is higher than 100, owing to that green-yellow and red colors are slightly oversaturated (Figure S6a–S6c). In contrast, R_g for WTLED A and F is 100, which perfectly mimic the ideal lighting source. At high CCT, R_g of all samples is higher than 100, which can be attributed to obvious oversaturation of green-yellow and violet-blue colors (Figure S6d–S6f). These results above indicate that WTLED F excited by TLED with highest intensity ratio, shows the best R_g–R_f scores among four samples regardless of CCT, enabling the color reproduction of objects when illuminated under sunlight.

Author Manuscript

This article is protected by copyright. All rights reserved.

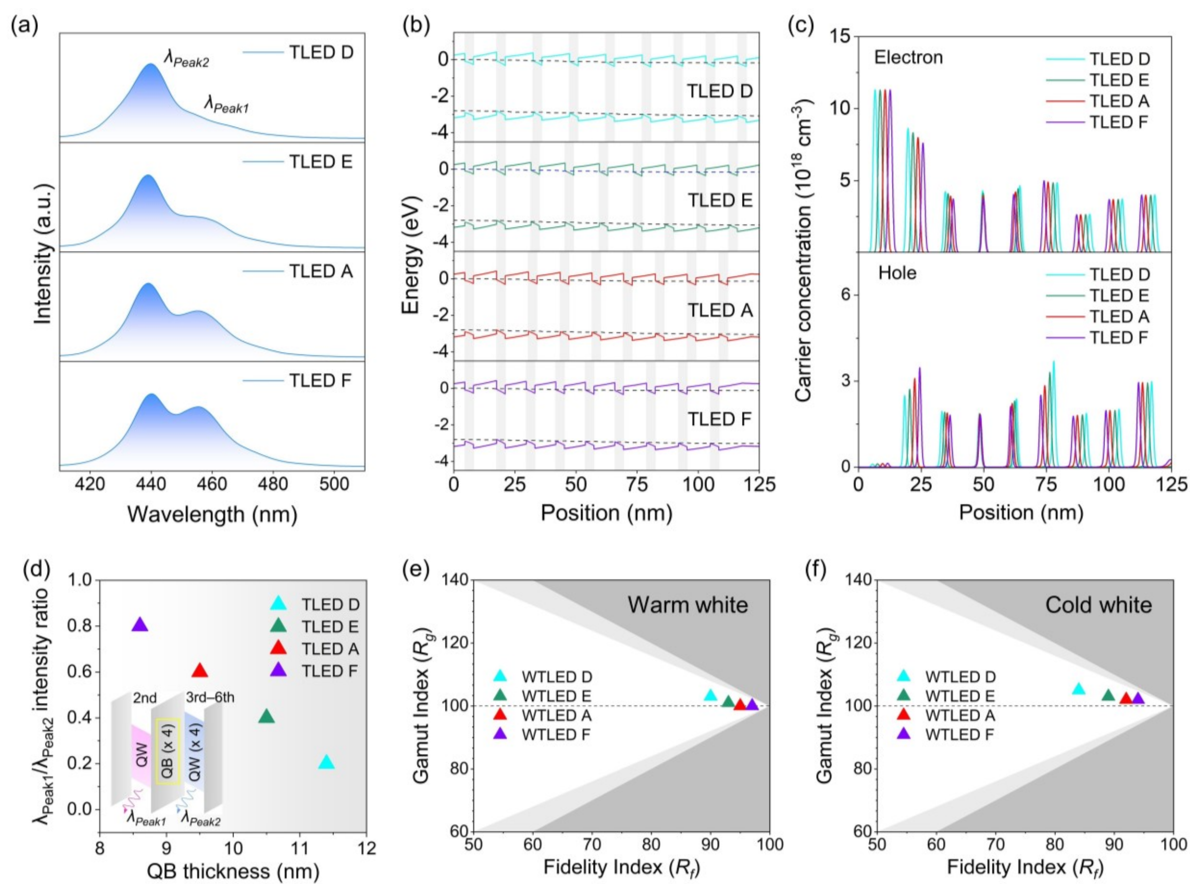

Figure 4. a) EL spectra of TLEDs with varying intensity ratios. The TLEDs are designed to feature $\Delta\lambda$ of 16~18 nm. b) Energy band diagram of MQWs for TLED samples. c) Numerical simulation of carrier concentration of TLED samples. The carrier concentration profiles were purposely shifted for comparison. d) Relationship between QB thickness and $\lambda_{Peak1}/\lambda_{Peak2}$ intensity ratio. IES TM-30-18 R_f–R_g of the fabricated e) warm and f) cold WTLEDs.

Table 1 and S4 have summarized key features of high CRI phosphor-converted WLEDs, which utilized different LED excitation sources and phosphors. Compared with previous report, we propose a facile and universal strategy to fabricate full-spectrum warm and cold WLEDs with excellent performance, where single excitation source with a minimum number of commercial phosphors is employed, even without utilization or optimization of novel efficient phosphors reported.

Author M

This article is protected by copyright. All rights reserved.

Table 1 Comparison of WLEDs based on III-nitride excitation source reported previously

Method	CRI	R_f–R_g	CCT (K)	Luminous efficacy (lm/W)	Ref.
Blue LED + $CsPb(Br_{0.75}, Cl_{0.25})_3$, $CsPbBr_3$, $CsPb(Br_{0.65}, I_{0.35})_3$, $CsPb(Br_{0.6}, I_{0.4})_3$, $CsPb(Br_{0.5}, I_{0.5})_3$, and $CsPb(Br_{0.35}, I_{0.65})_3$	96	(93.6, 100.8)	2605	43.3	[21]
Trichromatic LED + LuAG and $CaAlSiN_3$: Eu^{2+}	97.4	(97,100)	2807	124.35	This work
Trichromatic LED + (SrCa)$AlSiN_3$:Eu^{2+}	92	N.A.	2900	100	[12c]
2 Blue LEDs and 1 Ultraviolet (UV) LED + GNYAG3757 and R6634	97.3	(93, 104)	2906	100.12	[17]
Dichromatic LED + YAG and nitride composition	98.6	N.A.	~3400	4	[23]
UV LED + (Sr, Ca)$AlSiN_3$:Eu^{2+}, $(C_6H_9N_2)_2MnBr_4$ and $BaMgAl_{10}O_{17}$:Eu^{2+}	97	(94.2, 99.5)	4245	0.18	[24]
Trichromatic LED + LuAG and $CaAlSiN_3$: Eu^{2+}	98.9	(97, 99)	4954	145.26	This work
UV LED chip + theobromine dye styrene-butadiene-styrene composite	90	(90, 104)	5383	N.A.	[25]
Dichromatic LED + YAG: Ce^{3+}	91	N.A.	6500	58.3	[12d]

3. Conclusion

Author Manuscript

This article is protected by copyright. All rights reserved.

In summary, we have demonstrated monolithic integration of trichromatic MQWs structure on sapphire via bandgap engineering heteroepitaxial growth for efficient full-spectrum WLED. Comprehensive studies show that white light quality could be optimized by adjusting trichromatic MQWs including indium composition and QB thickness that results in different wavelength intervals and intensity ratios. Together with numerical analysis that reveals the carrier transport behavior affected by quantum structure, relatively small wavelength interval benefits warm white light, while the contrary is the case for the cold white light. In addition, intensity ratio is also found to influence color rendering ability. In detail, relatively large value enables better WLED performance towards both warm and cold sunlight. Such superior excitation source is thus employed to achieve highly efficient WLEDs with excellent R_a above 97, R_f of 97, and R_g of 100 at low CCT, and R_a above 98, R_f of 97, and R_g of 99 at high CCT. Moreover, the fabricated WLED devices not only exhibit high luminous efficacy above 120 and 140 lm/W for warm and cold white light emission, respectively, but also features broadband and continuous emission spectra with reduced blue light hazard that is inevitably encountered in commercial phosphor-converted WLEDs. We believe that our full-spectrum WLED platform initiates a more emphasis on the monolithically integrated excitation source on sapphire via nanoscale bandgap engineering growth, and offers a facile path for the successful fabrication of next-generation lighting sources, eventually broadening the application of bandgap engineering in various electronics and optoelectronics.

4. Experimental Section/Methods

Growth and Device Fabrication: GaN-based LEDs acting as excitation source were grown on the *c*-plane patterned sapphire substrate (PSS) using MOCVD. Trimethylindium (TMGa), triethylgallium (TEGa), trimethylgallium (TMIn), and trimetlhylaluminum (TMAl) were used as metal-organic precursor sources and ammonia (NH_3) was the nitrogen precursor. Hydrogen (H_2) and nitrogen (N_2) were used as carrier gases during the epitaxial growth process. Silane and bis-cyclopentadienyl magnesium were the *n*-dopant and *p*-dopant sources, respectively. The epitaxial structure of LED started from a 25-nm-thick GaN buffer layer grown on PSS, then a 3-μm-thick undoped GaN layer was grown at 1050 °C, and a Si-doped *n*-GaN layer (Si doping = 1.5×10^{19} cm^{-3}) with a thickness of 2.5

Author Manuscript

This article is protected by copyright. All rights reserved.

μm was grown at 1100 ℃, followed by six pairs of 1.5 nm InGaN/9 nm GaN superlattices (SL) grown at 900 ℃. The active region consists of nine pairs of 3.5 nm $In_xGa_{1-x}N$/9.5 nm GaN MQWs, where trichromatic InGaN QWs with increasing wavelengths were grown at decreasing temperature from 796 ℃ to 780 ℃ and GaN was grown at 800 ℃. Then, a 25 nm-thick *p*-$Al_{0.2}Ga_{0.8}N$ electron blocking layer was deposited at 900 ℃, and finally the structure ended with a 50 nm-thick Mg-doped *p*-GaN layer (Mg doping = 3×10^{19} cm^{-3}, 800 ℃) and a 3-nm-thick Mg-doped p^+-GaN layer (Mg doping = 6×10^{19} cm^{-3}, 1000 ℃). MLED has the same structure as TLED, except MQWs with uniform indium composition for the former. The growth rate of GaN quantum barrier layers in all samples is 0.0317 nm/s and different barrier thickness can be obtained by adjusting the growth time.

To fabricate LED chips, the *n*-type mesa was defined through standard photolithography and inductively coupled plasma etching. Indium tin oxide (ITO) layer was then deposited on the p^+-GaN layer, which was followed by thermal annealing at 350 °C for 30 min in a N_2 atmosphere. Subsequently, Cr/Pt/Au multiple metal layers were deposited via e-beam evaporation to form the *p*- and *n*-type electrodes. Finally, the LED wafers were diced into chips with dimensions of 26 mil × 30 mil.

Garnet green phosphor (LuAG) and red phosphor ($CaAlSiN_3$: Eu^{2+}) dispersed in epoxy resin and then WLEDs were prepared by coating LED chips with the resin. By optimizing the mixing ratio of phosphors, devices emitting warm and cold white light were realized.

Characterization: X-ray diffraction (XRD) measurement was performed using a PANalytical X'Pert Pro MRD diffractometer with a CuKα X-ray source. The epitaxial structure was characterized using a Talos F200X transmission electron microscopy (TEM). An integrating sphere spectrometer system (CAS 140CT, Instrument Systems, Germany) was used to measure the optoelectronics properties of fabricated WLEDs under a forward-bias current of 60 mA at room temperature.

Numerical simulation: Carrier distribution in the active region was calculated using a carrier transport model implemented software SiLENSe 5.14 (STR Software Inc.). The model took the strain and the associated piezoelectric effects into account and solved the Schrödinger, Poisson, and continuity equations with proper boundary conditions. The electron and hole mobilities were set to

Author Manuscript

This article is protected by copyright. All rights reserved.

100 and 5 $cm^2/(V s)$, respectively. The InGaN/GaN band offset ratio (ΔE_c: ΔE_v) was set to 0.7: 0.3. The structural parameters used in the simulation were consistent with those of the actual LEDs.

Supporting Information

Supporting Information is available from the Wiley Online Library or from the author.

Acknowledgements

This research was funded by the National Natural Science Foundation of China (Grant Nos. 52075394 and 51675386), the National Key R&D Program of China (No. 2021YFB3600204), and the National Youth Talent Support Program.

Conflict of Interest

The authors declare no conflict of interest.

Contributions

B. J. Fan and X. Y. Zhao contributed equally to this work. The manuscript was written through contributions of all authors.

Received: ((will be filled in by the editorial staff))

Revised: ((will be filled in by the editorial staff))

Published online: ((will be filled in by the editorial staff))

Author Manuscript

This article is protected by copyright. All rights reserved.

References

[1] a) T. D. Moustakas, R. Paiella, Reports on Progress in Physics **2017**, 80, 106501; b) Y. Yu, T. Wang, X. Chen, L. Zhang, Y. Wang, Y. Niu, J. Yu, H. Ma, X. Li, F. Liu, G. Deng, Z. Shi, B. Zhang, X. Wang, Y. Zhang, Light: Science & Applications **2021**, 10, 117; c) H. Hu, B. Tang, H. Wan, H. Sun, S. Zhou, J. Dai, C. Chen, S. Liu, L. J. Guo, Nano Energy **2020**, 69, 104427; d) D. Wang, X. Liu, Y. Kang, X. Wang, Y. Wu, S. Fang, H. Yu, M. H. Memon, H. Zhang, W. Hu, Z. Mi, L. Fu, H. Sun, S. Long, Nature Electronics **2021**, 4, 645; e) S. Zhou, X. Liu, H. Yan, Z. Chen, Y. Liu, S. Liu, Optics Express **2019**, 27, A669; f) Y. Lu, X. Ma, L. Yang, B. Hou, M. Mi, M. Zhang, J. Zheng, H. Zhang, Y. Hao, IEEE Electron Device Letters **2018**, 39, 811; g) X. Qiu, Y. Zhang, S. Hang, Y. Gao, Z. H. Zhang, Optics Express **2020**, 28.

[2] a) D. Li, S. Liu, Z. Qian, Q. Liu, K. Zhou, D. Liu, S. Sheng, B. Sheng, F. Liu, Z. Chen, P. Wang, T. Wang, X. Rong, R. Tao, J. Kang, F. Chen, J. Kang, Y. Yuan, Q. Wang, M. Sun, W. Ge, B. Shen, P. Tian, X. Wang, Advanced Materials **2022**, 34, 2109765; b) Z. Liu, B. Liu, F. Ren, Y. Yin, S. Zhang, M. Liang, Z. Dou, Z. Liu, S. Yang, J. Yan, T. Wei, X. Yi, C. Wu, T. Guo, J. Wang, Y. Zhang, J. Li, P. Gao, Small **2022**, 18, 2200057; c) X. M. Cai, Z. W. Zheng, H. Long, L. Y. Ying, B. P. Zhang, Applied Physics Letters **2018**, 112, 161102.

[3] a) J. Ye, S. Gu, S. Zhu, T. Chen, L. Hu, F. Qin, R. Zhang, Y. Shi, Y. Zheng, Journal of Crystal Growth **2002**, 243, 151; b) H. Sun, K.-H. Li, C. G. T. Castanedo, S. Okur, G. S. Tompa, T. Salagaj, S. Lopatin, A. Genovese, X. Li, Crystal Growth & Design **2018**, 18, 2370; c) T. Zhang, Q. Cheng, Y. Li, Z. Hu, J. Ma, Y. Yao, Y. Zhang, Y. Zuo, Q. Feng, Y. Zhang, H. Zhou, J. Ning, C. Zhang, J. Zhang, Y. Hao, Scripta Materialia **2022**, 213, 114623.

[4] a) G. Migliato Marega, Y. Zhao, A. Avsar, Z. Wang, M. Tripathi, A. Radenovic, A. Kis, Nature **2020**, 587, 72; b) W. Meng, F. Xu, Z. Yu, T. Tao, L. Shao, L. Liu, T. Li, K. Wen, J. Wang, L. He, L. Sun, W. Li, H. Ning, N. Dai, F. Qin, X. Tu, D. Pan, S. He, D. Li, Y. Zheng, Y. Lu, B. Liu, R. Zhang, Y. Shi, X. Wang, Nature Nanotechnology **2021**, 16, 1231; c) D. Andrzejewski, H. Myja, M. Heuken, A. Grundmann, H. Kalisch, A. Vescan, T. Kümmell, G. Bacher, ACS Photonics **2019**, 6, 1832; d) R. S. Lee, D. Kim, S. A. Pawar, T. Kim, J. C. Shin, S.-W. Kang, ACS Nano **2019**, 13, 642; e) Q. Cheng, J. Pang, D. Sun, J. Wang, S. Zhang, F. Liu, Y. Chen, R. Yang, N. Liang, X. Lu, Y. Ji, J. Wang, C. Zhang, Y. Sang, H. Liu, W. Zhou, InfoMat **2020**, 2, 656.

[5] a) S. Zhou, X. Zhao, P. Du, Z. Zhang, X. Liu, S. Liu, L. J. Guo, Nanoscale **2022**, 14, 4887; b) X. Zhao, B. Tang, L. Gong, J. Bai, J. Ping, S. Zhou, Applied Physics Letters **2021**, 118, 182102; c) D. Iida, Z. Zhuang, P. Kirilenko, M. Velazquez-Rizo, K. Ohkawa, Applied Physics Letters **2020**, 117, 172103.

[6] a) S. F. Chichibu, A. Uedono, T. Onuma, B. A. Haskell, A. Chakraborty, T. Koyama, P. T. Fini, S. Keller, S. P. DenBaars, J. S. Speck, U. K. Mishra, S. Nakamura, S. Yamaguchi, S. Kamiyama, H. Amano, I. Akasaki, J. Han, T. Sota, Nature Materials **2006**, 5, 810; b) E. F. Schubert, K. Kim Jong, Science **2005**,

Author Manuscript

This article is protected by copyright. All rights reserved.

308, 1274; c) M. H. Crawford, IEEE Journal of Selected Topics in Quantum Electronics **2009**, 15, 1028; d) J. Cho, J. H. Park, J. K. Kim, E. F. Schubert, Laser & Photonics Reviews **2017**, 11, 1600147.

[7] a) Y. Narukawa, M. Ichikawa, D. Sanga, M. Sano, T. Mukai, Journal of Physics D: Applied Physics **2010**, 43, 354002; b) J. J. Wierer Jr, J. Y. Tsao, D. S. Sizov, Laser & Photonics Reviews **2013**, 7, 963.

[8] a) Z. Ma, Z. Shi, D. Yang, Y. Li, F. Zhang, L. Wang, X. Chen, D. Wu, Y. Tian, Y. Zhang, L. Zhang, X. Li, C. Shan, Advanced Materials **2021**, 33, 2001367; b) Y. Touitou, A. Reinberg, D. Touitou, Life Sciences **2017**, 173, 94; c) L. Tähkämö, T. Partonen, A.-K. Pesonen, Chronobiology International **2019**, 36, 151.

[9] a) S. Huang, M. Shang, Y. Yan, Y. Wang, P. Dang, J. Lin, Laser & Photonics Reviews **2022**, n/a, 2200473; b) J. Hye Oh, S. Ji Yang, Y. Rag Do, Light: Science & Applications **2014**, 3, e141; c) N. Zhang, Z. Wang, J. Zhao, D. Wang, X. Liu, Z. Yang, P. Li, ACS Applied Electronic Materials **2021**, 3, 1115.

[10] a) L. Wang, R.-J. Xie, Y. Li, X. Wang, C.-G. Ma, D. Luo, T. Takeda, Y.-T. Tsai, R.-S. Liu, N. Hirosaki, Light: Science & Applications **2016**, 5, e16155; b) P. Pust, V. Weiler, C. Hecht, A. Tücks, A. S. Wochnik, A.-K. Henß, D. Wiechert, C. Scheu, P. J. Schmidt, W. Schnick, Nature Materials **2014**, 13, 891; c) M. Zhao, H. Liao, L. Ning, Q. Zhang, Q. Liu, Z. Xia, Advanced Materials **2018**, 30, 1802489; d) H. Zhu, C. C. Lin, W. Luo, S. Shu, Z. Liu, Y. Liu, J. Kong, E. Ma, Y. Cao, R.-S. Liu, X. Chen, Nature Communications **2014**, 5, 4312; e) Y. Wei, Z. Cheng, J. Lin, Chemical Society Reviews **2019**, 48, 310; f) J. Ziegler, S. Xu, E. Kucur, F. Meister, M. Batentschuk, F. Gindele, T. Nann, Advanced Materials **2008**, 20, 4068; g) Q. Mo, C. Chen, W. Cai, S. Zhao, D. Yan, Z. Zang, Laser & Photonics Reviews **2021**, 15, 2100278; h) S. Abe, J. J. Joos, L. I. D. J. Martin, Z. Hens, P. F. Smet, Light: Science & Applications **2017**, 6, e16271; i) H. V. Demir, S. Nizamoglu, T. Erdem, E. Mutlugun, N. Gaponik, A. Eychmüller, Nano Today **2011**, 6, 632.

[11] a) H. Amano, N. Sawaki, I. Akasaki, Y. Toyoda, Applied Physics Letters **1986**, 48, 353; b) H. Amano, M. Kito, K. Hiramatsu, I. Akasaki, Japanese Journal of Applied Physics **1989**, 28, L2112; c) S. Nakamura, T. Mukai, M. Senoh, Applied Physics Letters **1994**, 64, 1687.

[12] a) R. Mirhosseini, M. F. Schubert, S. Chhajed, J. Cho, J. K. Kim, E. F. Schubert, Optics Express **2009**, 17, 10806; b) R. Charash, P. P. Maaskant, L. Lewis, C. McAleese, M. J. Kappers, C. J. Humphreys, B. Corbett, Applied Physics Letters **2009**, 95, 151103; c) J.-K. Sheu, F.-B. Chen, Y.-C. Wang, C.-C. Chang, S.-H. Huang, C.-N. Liu, M.-L. Lee, Optics Express **2015**, 23, A232; d) Q.-R. Yan, Y. Zhang, S.-T. Li, Q.-A. Yan, P.-P. Shi, Q.-L. Niu, M. He, G.-P. Li, J.-R. Li, Opt. Lett. **2012**, 37, 1556; e) Q. Lv, J. Liu, C. Mo, J. Zhang, X. Wu, Q. Wu, F. Jiang, ACS Photonics **2019**, 6, 130; f) D. S. Arteev, S. Y. Karpov, A. V. Sakharov, A. E. Nikolaev, S. O. Usov, W. V. Lundin, A. F. Tsatsulnikov, Semiconductor Science and Technology **2020**, 35, 045017.

Author Manuscript

This article is protected by copyright. All rights reserved.

[13] a) S. Q. Zhou, M. F. Wu, L. N. Hou, S. D. Yao, H. J. Ma, R. Nie, Y. Z. Tong, Z. J. Yang, T. J. Yu, G. Y. Zhang, Journal of Crystal Growth **2004**, 263, 35; b) M. A. Moram, M. E. Vickers, Reports on Progress in Physics **2009**, 72, 036502.

[14] a) J. Nishio, L. Sugiura, H. Fujimoto, Y. Kokubun, K. Itaya, Applied Physics Letters **1997**, 70, 3431; b) M. E. Vickers, M. J. Kappers, T. M. Smeeton, E. J. Thrush, J. S. Barnard, C. J. Humphreys, Journal of Applied Physics **2003**, 94, 1565; c) D. G. Zhao, D. S. Jiang, L. C. Le, L. L. Wu, L. Li, J. J. Zhu, H. Wang, Z. S. Liu, S. M. Zhang, Q. J. Jia, H. Yang, Journal of Alloys and Compounds **2012**, 540, 46; d) F. Jiang, J. Zhang, L. Xu, J. Ding, G. Wang, X. Wu, X. Wang, C. Mo, Z. Quan, X. Guo, C. Zheng, S. Pan, J. Liu, Photon. Res. **2019**, 7, 144.

[15] J. H. Park, D. Y. Kim, E. F. Schubert, J. Cho, J. K. Kim, ACS Energy Letters **2018**, 3, 655.

[16] A. G. Bispo-Jr, L. F. Saraiva, S. A. M. Lima, A. M. Pires, M. R. Davolos, Journal of Luminescence **2021**, 237, 118167.

[17] Y. N. Ahn, K. D. Kim, G. Anoop, G. S. Kim, J. S. Yoo, Scientific Reports **2019**, 9, 16848.

[18] C. Li, M. Ronnier Luo, G. Cui, C. Li, Coloration Technology **2011**, 127, 129.

[19] A. Žukauskas, R. Vaicekauskas, P. Vitta, A. Tuzikas, A. Petrulis, M. Shur, Optics Express **2012**, 20, 5356.

[20] a) I. TM, New York, NY: The Illuminating Engineering Society of North America. 26p **2015**; b) I. ANSI, The Illuminating Engineering Society of North America **2018**.

[21] H. C. Yoon, J. H. Oh, S. Lee, J. B. Park, Y. R. Do, Scientific Reports **2017**, 7, 2808.

[22] a) G. Tao, X. Zhao, S. Zhou, Opt. Lett. **2021**, 46, 4593; b) C. Chu, D. Zhang, H. Shao, J. Che, K. Tian, Y. Zhang, Z.-H. Zhang, Opt. Mater. Express **2021**, 11, 1713.

[23] I. E. Titkov, A. Yadav, S. Y. Karpov, A. V. Sakharov, A. F. Tsatsulnikov, T. J. Slight, A. Gorodetsky, E. U. Rafailov, Laser & Photonics Reviews **2016**, 10, 1031.

[24] J. He, H. Zhao, X. Hu, Z. Fang, J. Wang, R. Zhang, G. Zheng, B. Zhou, F. Long, The Journal of Physical Chemistry C **2021**, 125, 22898.

[25] Y. Huang, T. A. Cohen, C. K. Luscombe, Advanced Sustainable Systems **2022**, 6, 2000300.

Author Manuscript

This article is protected by copyright. All rights reserved.

Monolithically Integrating III-Nitride Quantum Structure for Full-Spectrum White LED via Bandgap Engineering Heteroepitaxial Growth

*Benjie Fan[1], Xiaoyu Zhao[1], Jingqiong Zhang, Yuechang Sun, Hongzhi Yang, L. Jay Guo, and Shengjun Zhou**

B. J. Fan, J. Q. Zhang, H. Z. Yang

Kaistar Lighting (Xiamen) Co., Ltd., Xiamen 361000, P. R. China

X. Y. Zhao, Y. C. Sun, S. J. Zhou
Center for Photonics and Semiconductors, School of Power and Mechanical Engineering, Wuhan University, Wuhan 430072, P. R. China

E-mail: zhousj@whu.edu.cn

L. J. Guo

Department of Electrical Engineering and Computer Science, University of Michigan,

Ann Arbor, MI, 48109, USA

[1]*These authors contributed equally to this work.*

** Corresponding author.*

E-mail address: zhousj@whu.edu.cn (Shengjun Zhou).

Author Manuscript

This article is protected by copyright. All rights reserved.

This work reports efficient full-spectrum WLED excited by monolithically integrated III-nitride quantum structure, where trichromatic multiple quantum wells are constructed by bandgap engineering heteroepitaxy growth, allowing flexible manipulation of carrier transport behavior. With commercial green-red phosphor mixture, the fabricated WLEDs achieve broadband spectra with low-ratio blue component, superior color rendering and high luminous efficacy at different correlated color temperatures.

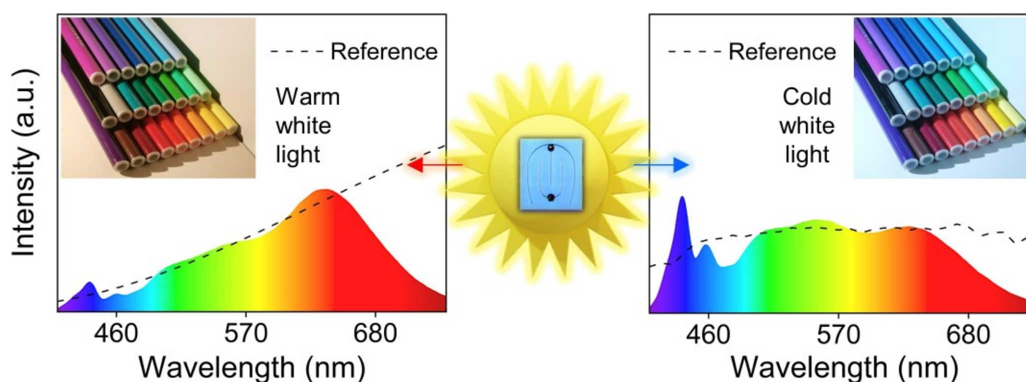

Author Manuscript

This article is protected by copyright. All rights reserved.